

Locally Enhanced and Tunable Optical Chirality in Helical Metamaterials

Philipp Gutsche ^{1,*}, Raquel Mäusle ¹ and Sven Burger ^{1,2}

¹ Zuse Institute Berlin, Takustr. 7, 14195 Berlin, Germany; maeusle@zib.de (R.M.); burger@zib.de (S.B.)

² JCMwave GmbH, Bolivarallee 22, 14050 Berlin, Germany

* Correspondence: gutsche@zib.de; Tel.: +49-30-841-85-203

Received: 31 October 2016; Accepted: 18 November 2016; Published: 23 November 2016

Abstract: We report on a numerical study of optical chirality. Intertwined gold helices illuminated with plane waves concentrate right and left circularly polarized electromagnetic field energy to sub-wavelength regions. These spots of enhanced chirality can be smoothly shifted in position and magnitude by varying illumination parameters, allowing for the control of light-matter interactions on a nanometer scale.

Keywords: metamaterials; optical chirality; computational nano-optics

1. Introduction

Helical metamaterials strongly impact the optical response of incident circularly (CPL) and linearly polarized light. They serve as efficient circular polarizers [1] and are candidates for chiral near-field sources [2]. Both, advancement of fabrication techniques [3–5] and design which employs fundamental physical properties [6] have significantly increased the performance of these complex structures.

Most experimental, numerical and theoretical studies focus on the far-field response of helical metamaterials. Nevertheless, near-field interaction of light and chiral matter is expected to be enhanced in chiral near-fields. Recently, the quantity of optical chirality has been introduced quantifying this phenomenon [7]. In the weak-coupling regime, the interplay of electromagnetic fields and chiral molecules, which are not superimposable with their mirror image, is directly proportional to this near-field measure [8].

Here, we use the concept of circularly polarized energy (CPE) which follows from the relation of optical chirality and electromagnetic field energy for lossless isotropic media [9]. We recapitulate the definitions of right and left CPE parts [10] and give a novel formal derivation of conservation of optical chirality in arbitrary space. The numerically investigated metamaterial consists of intertwined and tapered gold 3-helices. We observe subwavelength concentration of optical chirality density enhancement of more than a factor of four. Spatial control on a range of 1 μm is achieved while maintaining stable near-field intensities.

2. Optical Chirality and Circularly Polarized Energy

Analyzing light-matter interaction is mostly done with the help of electric and magnetic dipole moments of matter coupling to electric and magnetic parts of light, respectively. Emerging interest in specifically chiral matter yielded the introduction of the optical chirality density $\chi = \epsilon_0/2E \cdot (\nabla \times E) + 1/(2\mu_0)B \cdot (\nabla \times B)$ [7] with the electric field E , the magnetic flux density B , vacuum permittivity ϵ_0 and permeability μ_0 .

This time-even pseudoscalar resembles symmetry properties of chiral shapes: it changes sign under spatial inversion but not under time reversal. It occurs together with the mixed electric-magnetic dipole moment in the absorption rate of molecules and represents especially coupling of electromagnetic fields to chiral molecules. Furthermore, it satisfies the conservation

law $\partial_t \chi + \nabla \cdot \Sigma = 0$ with its flux $\Sigma = 1/2[E \times (\nabla \times B) - B \times (\nabla \times E)]$ in source-free, isotropic and homogeneous space.

Recently, this conservation law has been extended to arbitrary source- and material-distributions [10,11]. The occurring modified definitions of chiral quantities follow directly from Poynting's theorem. Formally, the relation $f : \mathbf{a} \cdot \mathbf{b} \mapsto 1/2[(\nabla \times \mathbf{a}) \cdot \mathbf{b} + \mathbf{a} \cdot (\nabla \times \mathbf{b})]$ acting on a scalar product $\mathbf{a} \cdot \mathbf{b}$ transforms conventional energy to chirality conservation:

$$f \{ \partial_t U + \nabla \cdot \mathbf{S} = \mathbf{J} \cdot \mathbf{E} \} \mapsto \partial_t \chi + \nabla \cdot \Sigma = 1/2 [(\nabla \times \mathbf{J}) \cdot \mathbf{E} + \mathbf{J} \cdot (\nabla \times \mathbf{E})], \quad (1)$$

where $U = U_e + U_m = 1/2(\mathbf{E} \cdot \mathbf{D} + \mathbf{H} \cdot \mathbf{B})$ is the field energy consisting of an electric and magnetic part, respectively. The electric displacement field is $\mathbf{D} = \epsilon \mathbf{E}$ and $\mathbf{B} = \mu \mathbf{H}$ with the magnetic field \mathbf{H} . \mathbf{J} is the free current density and $\mathbf{S} = \mathbf{E} \times \mathbf{H}$ is the energy flux.

Here, we study monochromatic fields governed by Maxwell's equations [12]. We consider complex time-harmonic electric fields $\mathcal{E} = \mathbf{E} \exp(-i\omega t)$ with angular frequency $\omega = 2\pi\nu$. Complex-valued material parameters ϵ and μ account for losses and the time-averaged energy densities are denoted with \mathcal{U} . The time-harmonic optical chirality in free space reads $\mathfrak{X} = -\epsilon_0 \omega / 2 \operatorname{Im}(\mathcal{E}^* \cdot \mathcal{B})$ [13]. The generalized continuity Equation (2) introduces an electric \mathfrak{X}_e and magnetic \mathfrak{X}_m chirality density

$$\begin{aligned} \mathfrak{X}_e &= 1/8 [\mathcal{D}^* \cdot (\nabla \times \mathcal{E}) + \mathcal{E} \cdot (\nabla \times \mathcal{D}^*)], \quad \mathfrak{X}_m = 1/8 [\mathcal{H}^* \cdot (\nabla \times \mathcal{B}) + \mathcal{B} \cdot (\nabla \times \mathcal{H}^*)] \\ \mathfrak{S} &= 1/4 [\mathcal{E} \times (\nabla \times \mathcal{H}^*) - \mathcal{H}^* \times (\nabla \times \mathcal{E})] \end{aligned} \quad (2)$$

with $\mathfrak{X} = \mathfrak{X}_e + \mathfrak{X}_m$ and the optical chirality flux \mathfrak{S} .

The optical chirality is proportional to the difference of CPE in isotropic lossless materials with refractive index n and speed of light $c = c_0/n$ with vacuum value c_0 [9]. This gives rise to a basis change for the total energy \mathcal{U} from electric and magnetic parts to right \mathcal{U}_R and left \mathcal{U}_L circularly polarized parts:

$$\mathfrak{X}(x) = \frac{\omega n}{c_0} [\mathcal{U}_L(x) - \mathcal{U}_R(x)], \quad (3)$$

$$\mathcal{U}(x) = \mathcal{U}_L(x) + \mathcal{U}_R(x) = \mathcal{U}_e(x) + \mathcal{U}_m(x). \quad (4)$$

Accordingly, the left and right CPE components are derived from the optical chirality and energy densities as $\mathcal{U}_{L,R} = 1/2\{\mathcal{U} \pm c_0/(\omega n)\mathfrak{X}\}$. This picture enables the analysis of chiral near-fields with respect to their degree of local circular polarization. It is known that for chiral matter, the study of enhancement of chirality should be compared to both electric and magnetic energy [14]. Conventionally, design of nano-optical devices aims at increasing the local enhancement factor $\hat{\mathfrak{X}}(x) = \mathfrak{X}(x)/|\mathfrak{X}_0|$ with chirality \mathfrak{X}_0 of the incident light [13].

However, by studying CPE, both achiral and chiral effects are taken into account: In measurements investigating circular dichroism, the differential response of e.g., a chiral molecule to two distinct circular polarizations of the incident light is analyzed. In this manner, the coupling to chiral fields is separated from achiral coupling. The CPE complements this differential picture when studying near-fields of a single polarization state. If purely enhancement of optical chirality was analyzed in this situation, a simultaneous increase in the achiral response could be overseen.

Namely, an equal enhancement of optical chirality as well as electric and magnetic energy is generally possible, as shown in Equations (3) and (4). Chiral responses could be enhanced as much as the achiral ones. By employing the CPE analysis, an enhancement of only chiral coupling is clearly separated from high achiral fields. Since optical chirality arises from the difference of the generally independent variables \mathcal{U}_L and \mathcal{U}_R , these offer an additional degree of freedom for designing the desired field properties. Accordingly, the CPE is helpful for studying both the handedness and the enhancement of chiral near-fields and their interaction with different enantiomers of chiral matter.

3. Controllable Chiral Near-Fields in Helical Metamaterial

We propose to study light matter interactions in chiral near-fields in the vicinity of metal helices. These fields can be conveniently tuned locally and spectrally in order to perform spectroscopic measurements. We demonstrate this tunability in a numerical study within an array of intertwined right-handed helices. The geometry of the helix array follows a previously investigated setup [15] which was proposed as a broadband circular polarizer. Such devices showing chiral far-field responses are based on employing chiral resonances instead of separate electric and magnetic resonances [16]. Although in this study we investigate how the near-field properties depend on illumination parameters, we show that analyzing chiral rather than achiral field quantities is also beneficial in the vicinity of plasmonic structures.

Figure 1a shows a schematic view of the hexagonal unit cell of the helix array (pitch $p = 1 \mu\text{m}$): Three intertwined, tapered metal helices are placed on top of a glass substrate and surrounded by air. The refractive index n of the metal (gold) is given by a free-electron model with plasma frequency $\omega_{\text{PL}} = 1.37 \times 10^{16} \text{ rad/s}$ and collision frequency $\omega_{\text{col}} = 1.2 \times 10^{14} \text{ rad/s}$.

The helices' wire diameter is $d = 100 \text{ nm}$, their axial pitch $H = 1 \mu\text{m}$ and bottom and top radius $r_1 = 100 \text{ nm}$, $r_2 = 250 \text{ nm}$. In the simulations, the structure is illuminated from above with right/left circularly polarized plane waves (RCP/LCP) in the infrared spectral range, at inclination angle θ with respect to the surface normal (helix axis) and rotation angle ϕ with respect to the Γ -K direction of the array. Throughout this study, we set $\phi = 0$.

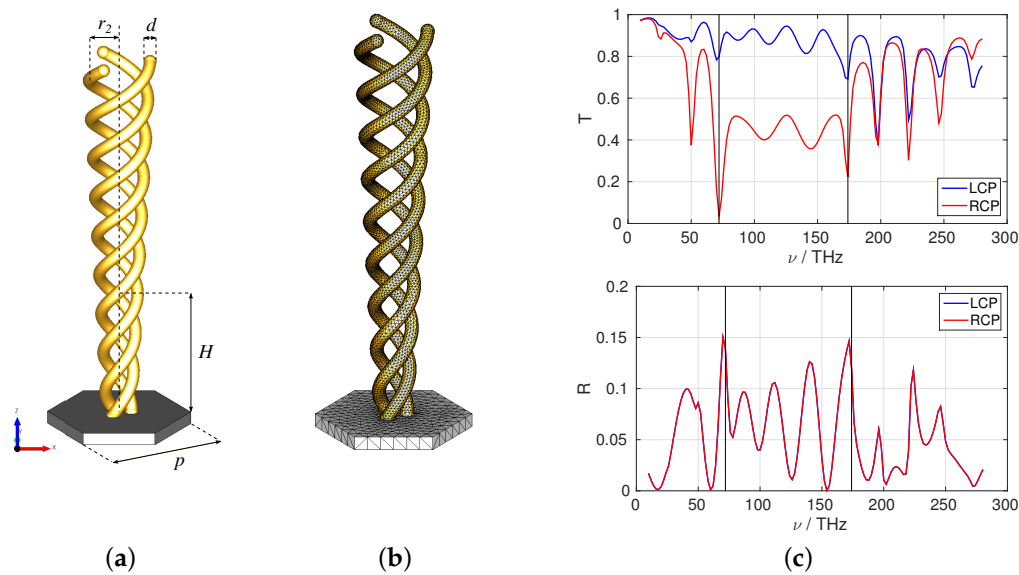


Figure 1. Tapered and intertwined gold 3-helices (a) and tetrahedral mesh (b) for finite-element method (FEM). Transmission T (c, top) and reflection R (c, bottom) spectra for normally incident right circularly polarized plane wave (RCP) (red) and left circularly polarized plane wave (LCP) (blue). Vertical black lines denote the band of suppressed T for RCP.

The structure is discretized with a tetrahedral mesh shown in Figure 1b. Near-field distributions are computed using the finite-element method (FEM) implemented in the software package *JCMsuite* [15]. Post-processes are used to determine electromagnetic field energies, chirality densities, transmission, reflection and other quantities. We have checked that the numerical relative error of the presented results is below one percent with respect to conservation of energy as well as conservation of optical chirality.

Figure 1c shows reflection and transmission spectra for $\theta = 0$. In accordance with symmetry considerations [6,17], the reflection for RCP and LCP is equal, leaving absorption as the major mechanism for filtering polarization. The structure is resonantly excited by RCP, yielding a band of

suppressed transmission from approximately 72 to 174 THz. Here, mean transmission coefficients are smaller than 0.45 for RCP and larger than 0.9 for LCP.

The tapering of the device results in a significantly increased operation bandwidth of the circular polarizer [6]. For the near-field analysis employed here, the angle of the tapering gives an additional degree of freedom for optimizing the position and magnitude of the observed enhancements. Especially for the tunability with respect to the obliqueness of the illumination described in Section 3.2, the tapering yields a constant volume of increased fields for different angles of incidence.

3.1. Frequency-Dependence of Local Enhancement

First, we analyze enhancement $\hat{\mathcal{U}}_i(z) = \mathcal{U}_i(z)/\mathcal{U}_{i,0}$ of the different energy quantities \mathcal{U}_i , given in Equation (4), compared to their free space value $\mathcal{U}_{i,0}$ as well as chirality enhancement $\hat{\chi}(z)$ on the helix axis (in z -direction). The helical metamaterial is illuminated with normally incident and right circularly polarized plane waves. The frequency ν is varied from 10 to 280 THz. As shown in Figure 2, several features arise in the near-fields.

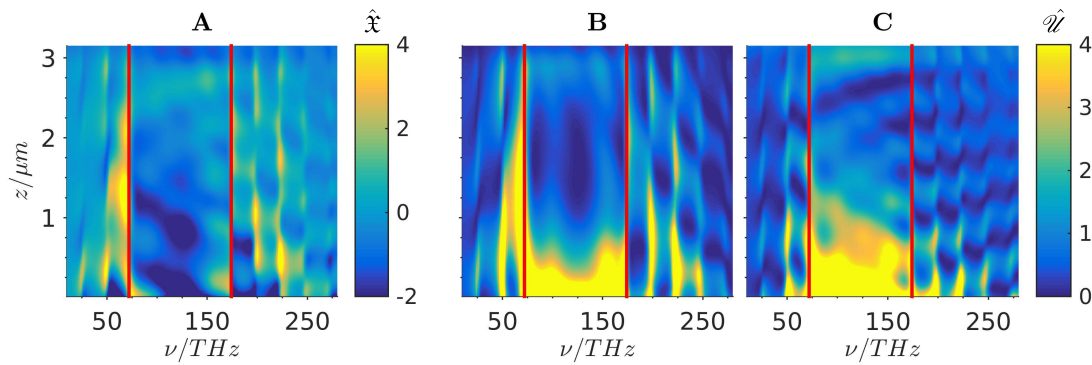


Figure 2. Spectral near-field response of a 3-helix array illuminated with normally incident RCP. Enhancements along the central z -axis are shown in pseudo-color representation as functions of frequency ν . Vertical red lines denote the band gap. (A): chirality enhancement $\hat{\chi}(z, \nu)$. (B,C): enhancement of left [right] circularly polarized energy $\hat{\mathcal{U}}_L(z, \nu)$ [$\hat{\mathcal{U}}_R(z, \nu)$]. Note the predominantly positive chirality at the left red line.

The highest magnitudes of optical chirality are located within $1.5 \mu\text{m}$ above the substrate in the center of the unit cell (Figure 2A). The band of suppressed transmission is depicted by vertical red lines. Within this band, two distinct and broadband enhancements are visible. Here, the incident optical chirality $\hat{\chi}_{\text{inc}} = -1$ is roughly doubled. The position of these low enhancements are spatially stable up to around 200 nm for variations of the frequency by 50 THz. This proposes an experimental setup wherein chiral enantiomers are placed in the center of the device coupling to locally enhanced chirality. Tuning the incident frequency amplifies signals of spectroscopy or enables spatial analysis of macro-molecules.

Stronger enhancements of optical chirality are observed outside the band of suppressed transmission. Above the band, field enhancements follow the oscillatory behavior of the transmission spectrum, whereas below the band, significant local chirality enhancement is observed by more than a factor of four at $\nu = 72$ THz. Note that the optical chirality changes sign compared to the incident RCP outside the band.

Analysis of the enhancement of the right and left CPE components is displayed in Figure 2B,C. It is much more prominent for resonant frequencies. An increase by more than four times is located less than 500 nm above the substrate within the full band. Above and below the band, CPE shows similar oscillatory behavior as optical chirality. The interplay of right and left CPE is the reason for the opposite handedness of the incident circular polarization outside the band.

As an example, we show in Figure 3 the local optical chirality (A) as well as right/left (B/C) and electric/magnetic (D/E) field energy enhancements for $\nu = 72$ THz. At this frequency, $\hat{\chi}(z, \nu)$ is maximal. The electric and magnetic field energy densities are inversely proportional as visible in Figure 3D,E, i.e., when \mathcal{U}_e is maximum, \mathcal{U}_m is minimum. The pronounced local chirality enhancement (A) is due to a high left CPE \mathcal{U}_L (B) while maintaining small \mathcal{U}_R (C).

In the picture of circularly polarized energy, these chiral near-fields are clearly understood since chirality is proportional to the difference of left and right CPE (3). However, they arise from the complex interplay of electric and magnetic field components. Their local phase relations are not directly accessible in the analysis of electric and magnetic energy densities. Nevertheless, these are the underlying reasons for the observed local chirality enhancement. From the point of view of chirality conservation, the incident chirality is locally converted [10] to left-handed CPE, resulting in the observed strong chiral near-fields.

It has been shown that the generation of the observed chiral near-fields can be explained by the current flows induced in helix wire [18]. The currents are circulating around the core of the helix, yielding a magnetic polarization. Additionally, some parts of the current flow parallel to the helix axis and induce an electric polarization. If these two contributions show the correct phase relation, the optical chirality density and accordingly the difference of the CPE parts is enhanced.

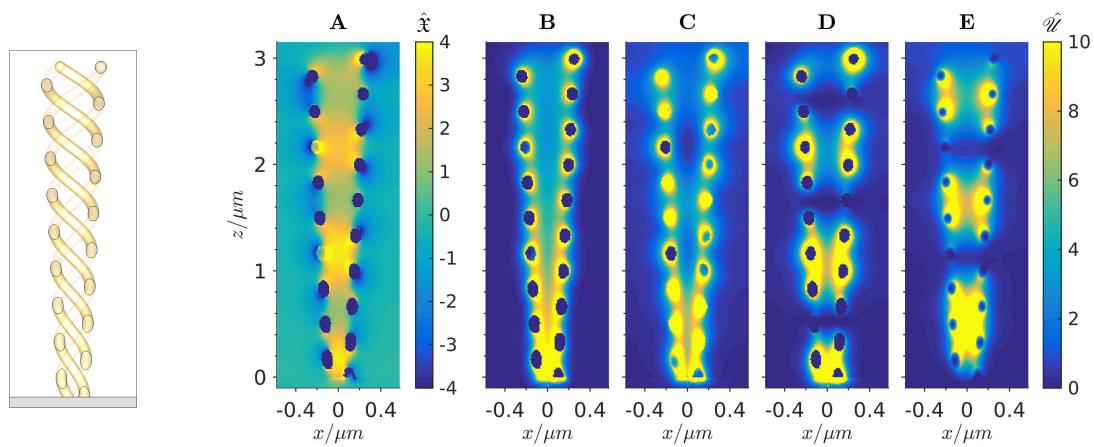


Figure 3. Near-fields of a 3-helix array at $\nu = 72$ THz illuminated with normally incident RCP. Enhancements compared to free space values in a xz -cross section (left) through the center of the unit cell are shown in pseudo-color representation. (A): chirality enhancement $\hat{\chi}(x, z)$; (B,C): enhancement of left [right] circularly polarized energy $\mathcal{U}_L(x, z)$ [$\mathcal{U}_R(x, z)$]; (D,E): enhancement of electric (magnetic) field energy $\mathcal{U}_e(x, z)$ [$\mathcal{U}_m(x, z)$].

3.2. Spatial Control of Chirality Enhancement by Tuning the Incidence Angle

Second, we study near-fields of the helical metamaterial when varying the angle of incidence θ at a fixed frequency $\nu = 128$ THz. The illuminating plane wave is left circularly polarized. Although the structure is close to transparent for normally incident LCP (Figure 1c), we observe high optical chirality and accurate control of the enhancement position.

In Figure 4A, the chirality enhancement on the symmetry axis of the device for $\theta \in [0^\circ, 45^\circ]$ is shown. The maximal enhancement is tunable between 1 and 2 μm above the substrate. It is nearly proportional to the incidence angle. In the range of 12° – 36° the magnitude of the local chirality is increased more than four times with a maximal value of more than six depicted by a red vertical line. This allows for easy experimental control of the position of high optical chirality at constant frequency and enables the spatial analysis of chiral molecules.

The strong chiral near-fields are due to an increased right CPE (Figure 4C) and a relatively low variation of the left-handed energy part (B). Analogous to the frequency-study in the previous section, the sign of the incident chirality is reversed. In Figure 5A–C, we show the spatial distribution of chirality and CPE enhancement for the angle with maximal chirality enhancement $\theta_{\max} = 31.5^\circ$. Here, the electric energy is much less increased whereas the magnetic part is strongly enhanced (not shown).

Again, the concept of circularly polarized energy is shown to be suitable for chiral phenomena: Although the electric dipole moment of most molecules is much stronger, the effect of magnetic coupling cannot be neglected for chiral phenomena [14]. On the other hand, studying CPE as given in Equation (4) is directly related to the interaction of light and chiral matter. This is underpinned by the close connection of chirality and the general polarization ellipse of local fields [19].

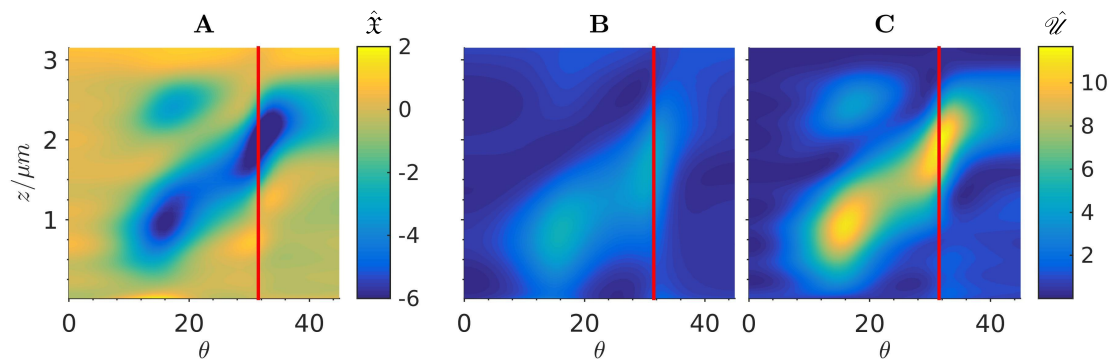


Figure 4. Near-field response of a 3-helix array illuminated with LCP at $\nu = 128$ THz. Enhancements along the central z -axis are shown in pseudo-color representation as functions of incidence angle θ . The vertical red line denotes the angle of incidence $\theta = 31.5^\circ$ with maximal $|\hat{\chi}| > 6$. (A): chirality enhancement $\hat{\chi}(z, \theta)$; (B,C): enhancement of left [right] circularly polarized energy $\mathcal{U}_L(z, \theta)$ [$\mathcal{U}_R(z, \theta)$]. Note the predominantly negative chirality when tuning the angle.

Finally, we investigate the unexpected behavior of reversing the sign of the incident optical chirality. As described in the previous section, this effect suggests a conversion mechanism of the metamaterial: Locally, chirality or the circular polarization of the incident light is converted into the opposite chirality. This occurs for resonant incident light showing low transmission.

We perform an analysis of accessible eigenmodes at the angle with maximal chirality enhancement θ_{\max} . This is done by solving the resonance problem of Maxwell's equations with Bloch conditions corresponding to this specific angle. Subsequently, the most suitable mode with local circular polarization and eigenfrequency similar to the externally excited near-field is chosen.

Generally, the coupling to all eigenmodes which overlap with the external field has to be taken into account for a full description of the device. Additional interference of the incident field and different modes might occur. However, in order to show that the tuning capabilities, with respect to the angle of incidence, are based on modes accessible only under oblique illumination, we analyze the eigenfield which is mostly excited.

In Figure 5A,D, we compare near-field chirality of the illumination with LCP with the corresponding eigenmode. Since its eigenfrequency and the frequency of the incident plane wave is equal, the incident light couples to this mode, although its local chirality is of opposite handedness. Accordingly, the observed chirality conversion mechanism occurs. We expect a similar behavior in the case of the frequency-dependent chirality enhancement in the previous section.

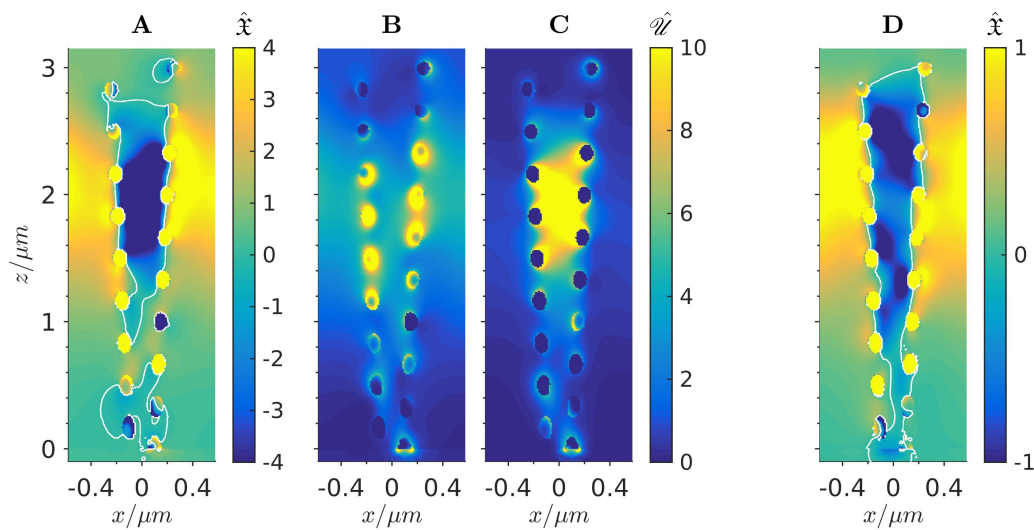


Figure 5. Comparison of near-field response for scattering (A–C) with LCP at $\nu = 128$ THz and $\theta = 31.5^\circ$ and resonance (D) computation with corresponding Bloch vector. Enhancements in a xz -cross section through the center of the unit cell are shown in pseudo-color representation. White lines depict zero chirality. (A,D): chirality enhancement $\hat{\chi}(x, z)$ from scattering [resonance] computation. (B,C): enhancement of left [right] circularly polarized energy $\hat{\mathcal{U}}_L(x, z)$ [$\hat{\mathcal{U}}_R(x, z)$] from scattering simulation.

4. Conclusions

In summary, metamaterials composed of intertwined and tapered 3-helices enable the control of the chiral optical near-fields both spatially and in magnitude. Variation of wavelength or the angle of incident CPL controls the vertical position in the range of micrometers of local chirality. Enhancement factors of up to six are obtained on the central axis of this device. The numerical analysis, with the help of CPE, simplifies the complex interplay of electromagnetic fields forming local circular polarization and gives design guidelines for chiral light-matter interactions.

We expect the two independent CPE components to offer more degrees of freedom for optimization of comparable devices than solely the quantity of optical chirality and have shown that the interplay of extrinsic chiral parameters, such as angle of incidence and intrinsic geometric chirality of e.g., tapered 3-helices, offer the ability to tune chiral near-fields.

Acknowledgments: We acknowledge support from the BMBF through project 13N13164, the Einstein Foundation Berlin through project ECMath-SE6, the DFG through SFB787-TP4 and the Freie Universität Berlin.

Author Contributions: All authors conceived the concept of the study and discussed the results. R.M. performed the simulations. P.G. wrote the paper with input from S.B. and R.M.

Conflicts of Interest: The authors declare no conflict of interest.

Abbreviations

The following abbreviations are used in this manuscript:

CPL	Circularly Polarized Light
CPE	Circularly Polarized Energy
RCP	Right Circularly Polarized Plane Wave
LCP	Left Circularly Polarized Plane Wave
FEM	Finite-Element Method

References

1. Gansel, J.K.; Thiel, M.; Rill, M.S.; Decker, M.; Bade, K.; Saile, V.; von Freymann, G.; Linden, S.; Wegener, M. Gold helix photonic metamaterial as broadband circular polarizer. *Science* **2009**, *325*, 1513–1515.
2. Schäferling, M.; Yin, X.; Engheta, N.; Giessen, H. Helical Plasmonic Nanostructures as Prototypical Chiral Near-Field Sources. *ACS Photonics* **2014**, *1*, 530–537.
3. Kaschke, J.; Wegener, M. Optical and Infrared Helical Metamaterials. *Nanophotonics* **2016**, *3*, 38.
4. Deng, J.; Fu, J.; Ng, J.; Huang, Z. Tailorable chiroptical activity of metallic nanospiral arrays. *Nanoscale* **2016**, *8*, 4504–4510.
5. Esposito, M.; Tasco, V.; Cuscunà, M.; Todisco, F.; Benedetti, A.; Tarantini, I.; Giorgi, M.D.; Sanvitto, D.; Passaseo, A. Nanoscale 3D Chiral Plasmonic Helices with Circular Dichroism at Visible Frequencies. *ACS Photonics* **2014**, *2*, 105–114.
6. Kaschke, J.; Gansel, J.K.; Wegener, M. On metamaterial circular polarizers based on metal N-helices. *Opt. Express* **2012**, *20*, 26012–26020.
7. Tang, Y.; Cohen, A.E. Optical Chirality and Its Interaction with Matter. *Phys. Rev. Lett.* **2010**, *104*, 163901.
8. Schäferling, M.; Engheta, N.; Giessen, H.; Weiss, T. Reducing the complexity: Enantioselective chiral near-fields by diagonal slit and mirror configuration. *ACS Photonics* **2016**, *3*, 1076–1084.
9. Bliokh, K.Y.; Nori, F. Characterizing Optical Chirality. *Phys. Rev. A* **2011**, *83*, 021803(R).
10. Gutsche, P.; Poulikakos, L.V.; Hammerschmidt, M.; Burger, S.; Schmidt, F. Time-harmonic optical chirality in inhomogeneous space. *Proc. SPIE* **2016**, 9756, 97560X.
11. Poulikakos, L.V.; Gutsche, P.; McPeak, K.M.; Burger, S.; Niegemann, J.; Hafner, C.; Norris, D.J. The Optical Chirality Flux as a Useful Far-Field Probe of Chiral Near Fields. *ACS Photonics* **2016**, *3*, 1619–1625.
12. Jackson, J.D. *Classical Electrodynamics*; Wiley: Hoboken, NJ 07030, 1998.
13. Schäferling, M.; Dregely, D.; Hentschel, M.; Giessen, H. Tailoring Enhanced Optical Chirality: Design Principles for Chiral Plasmonic Nanostructures. *Phys. Rev. X* **2012**, *2*, 031010.
14. Choi, J.S.; Cho, M. Limitations of a superchiral field. *Phys. Rev. A* **2012**, *86*, 063834.
15. Kaschke, J.; Blome, M.; Burger, S.; Wegener, M. Tapered N-helical metamaterials with three-fold rotational symmetry as improved circular polarizers. *Opt. Express* **2014**, *22*, 19936–19946.
16. Pendry, J. A chiral route to negative refraction. *Science* **2004**, *306*, 1353–1355.
17. Menzel, C.; Rockstuhl, C.; Lederer, F. Advanced Jones calculus for the classification of periodic metamaterials. *Phys. Rev. A* **2010**, *82*, 053811.
18. Demetriadou, A.; Oh, S.S.; Wuestner, S.; Hess, O. A tri-helical model for nanoplasmonic gyroid metamaterials. *New J. Phys.* **2012**, *14*, 083032.
19. Bauer, T.; Banzer, P.; Karimi, E.; Orlov, S.; Rubano, A.; Marrucci, L.; Santamato, E.; Boyd, R.W.; Leuchs, G. Observation of optical polarization Möbius strips. *Science* **2015**, *347*, 964–966.



© 2016 by the authors; licensee MDPI, Basel, Switzerland. This article is an open access article distributed under the terms and conditions of the Creative Commons Attribution (CC-BY) license (<http://creativecommons.org/licenses/by/4.0/>).